Coupling between cohesive element method and Node-to-segment contact algorithm : Implementation and application

Mohit Pundir, Guillaume Anciaux

Coupling between cohesive element method and Node-to-segment contact algorithm : Implementation and application

Mohit Pundir[a,], Guillaume Anciaux[a]

[a]*Computational Solid Mechanics Laboratory, ENAC, École Polytechnique Fédérale de Lausanne, CH-1015 Lausanne, Switzerland;*

Abstract

In materials, the evolution of crack surfaces is intimately linked with the self-contact oc-curing between them. The developed contact forces not only mitigate the effect of stress concentration at crack tip but also contribute significantly to the transfer of shear and normal stresses. In this paper, we present a numerical framework to study the simulta-neous process of fracture and self-contact between fracturing surfaces. The widely used approach, where contact constraints are enforced with the cohesive element *traction sepa-ration law*, is demonstrated to fail for relative displacements greater than the characteristic mesh length. A hybrid approach is proposed, which couples a *node-to-segment* contact algorithm with *extrinsic* cohesive elements. Thus, the fracture process is modeled with cohesive elements whereas the contact and the friction constraints are enforced through a *penalty-based* method. This hybrid cohesive-contact approach is shown to alleviate any mesh topology limitations, making it a reliable and physically-based numerical model for studying crack propagation along rough surfaces.

Keywords: Penalty-based contact, Cohesive element, Friction, Finite Element Method

1. Introduction

Failure in materials is most often attributed to micro-cracking mechanisms in the ma-terial. It has been well studied how the inherent presence of microscopic cracks and the stress concentration around them leads to crack growth and coalescence [1]. The merging of micro-cracks results in propagation of macro-cracks which finally lead to material fail-ure. Depending on the local stress state, the micro-cracks may come into contact leading to the development of residual stresses either due to friction, or due to the rough topology of crack faces. Such residual stresses significantly influence the stress at crack-tip. Thus, a holistic understanding of fracture mechanisms in material requires to model not only micro-cracking but also the contact occuring between cracked surfaces.

One of the widely used numerical approach stems from *cohesive zone models*. In front of the crack tip, there exists a small non-linear region where degradation of material takes place, which is denoted as the *fracture process zone*. It is within this region that the local micro-cracks initiate, propagate and coalesce (see Figure 1a). The cohesive zone models, first introduced by Dugdale and Barenblatt [2] in the 1960s, idealize the *fracture process zone* as a discrete interface (see Figure 1b) and the degradation behavior is defined by
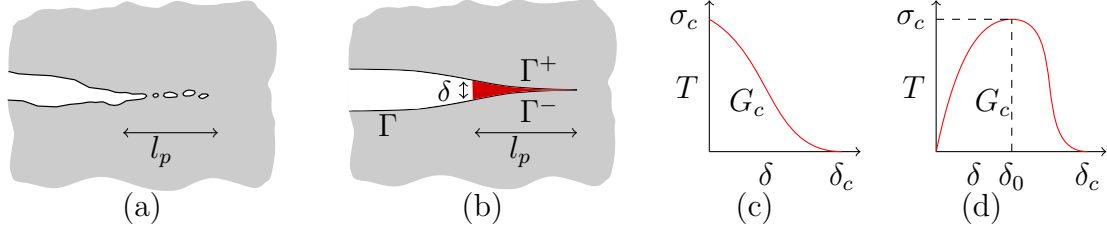

Figure 1: (a) Initiation, propagation and coalescence of micro-cracks in the fracture process zone represented as l_p (b) Idealization of crack and fracture process zone by *cohesive zone models*. Γ^+ represent the upper facet of a cohesive surface and Γ^- represents the lower facet of a cohesive surface. Γ represents a free boundary in the body (c) Cohesive traction T as a function of crack opening δ for an extrinsic approach (d) Cohesive traction law for an intrinsic approach.

the constitutive relation called the *Traction-Separation Law* (TLS) [3, 4, 5]. It relates the cohesive traction T along the interface to the relative displacement δ between the separated cohesive surfaces: $T = f(\delta)$. The TSL is controlled by the fracture energy G_c required to create a unit area of fully developed crack (see Figure 1):

$$G_c = \int_0^{\delta_c} f(\delta)d\delta \tag{1}$$

Over the years, the cohesive zone models have been adopted in various numerical frameworks, to simulate crack propagation [6, 7, 8, 9, 10]. With Finite Element modeling, interfacial cohesive elements are inserted in-between targeted finite elements. The insertion follows two distinguishable approaches: the *extrinsic* [3] and the *intrinsic* [11]. In the *intrinsic* approach, the cohesive elements are pre-inserted at the onset of the simulation, whereas in the *extrinsic* approach, a cohesive element is inserted only when the stress/traction along the interface exceeds the critical strength of the material. Furthermore, the choice of insertion affects the Traction Separation Law. For an *extrinsic* approach, the TSL is a monotonically decreasing function characterized by several parameters: the fracture energy G_c and the critical stress σ_c which triggers insertion (see Figure 1c). For the intrinsic approach, the TSL is a non-monotonic function characterized by three parameters: σ_c, G_c and δ_o, the crack opening at which the critical strength σ_c is reached (see Figure 1d). The effective crack opening δ is defined as $\delta = \sqrt{(\beta^2/\kappa^2)\delta_t^2 + \delta_n^2}$ where δ_n and δ_t represent normal and tangential openings. The parameter β provides a weighted coupling between normal and tangent modes, and κ becomes the ratio between critical energy release rate under Mode-I and Mode-II loadings $\kappa = G_{c,II}/G_{c,I}$. In this work, we employ *extrinsic* cohesive elements with a linear TSL which gives the cohesive traction vector during a loading path:

$$\underline{\boldsymbol{T}}_{coh} = \left(\frac{\beta^2}{\kappa}\delta_t\underline{\boldsymbol{t}} + \delta_n\underline{\boldsymbol{n}}\right)\frac{\sigma_c}{\delta}\left(1 - \frac{\delta}{\delta_c}\right) \tag{2}$$

where $\underline{\boldsymbol{t}}$ and $\underline{\boldsymbol{n}}$ are the tangent and normal vectors respectively, and where δ_c is the effective crack opening beyond which complete decohesion occurs. During unloading, the TSL follows a different path, which acknowledges δ_{max} as the maximum opening displacement

2

of all previous loading paths:

$$\underline{\boldsymbol{T}}_{coh} = \left(\frac{\beta^2}{\kappa} \delta_t \underline{\boldsymbol{t}} + \delta_n \underline{\boldsymbol{n}} \right) \frac{\sigma_c}{\delta_{\max}} \left(1 - \frac{\delta_{\max}}{\delta_c} \right) \quad \text{for } 0 < \delta < \delta_{\max} \tag{3}$$

which acknowledges irreversible damage.

Usually a penalty-based method is incorporated in the cohesive law to avoid interpenetration of facets (represented as Γ^+ and Γ^- in Figure 1b) when in compression [12, 7]. The normal contribution to the cohesive traction vector becomes

$$\underline{\boldsymbol{T}}_{coh}^n = \epsilon_n \delta_n \underline{\boldsymbol{n}} \quad \text{for } \delta_n < 0 \tag{4}$$

when $\delta_n < 0$, and where ϵ_n is the penalty parameter. However, there are a few limitations to such a method. As a pair of facets forming a cohesive element does not change over the time, this facet-to-facet approach necessarily assumes small displacements, i.e. $\delta \ll h$. Such a restriction limits the refinement of finite element meshes, for instance when it is required to represent small-scale surface features. It also requires the contact surfaces to be planar [13], which excludes the topologies observed when a complex crack network develops.

Over the years various approaches have been proposed to overcome the above mentioned difficulties. Snozzi et al. [5] employed an explicit enforcement of contact between cohesive elements using a decomposition contact response method [14] which imposes impenetrability condition directly on the displacements by conserving the linear and the angular momenta of the bodies. However, such a approach does not incorporate the work performed by contact forces and thus suffers from energy conservation problem [5]. Zhang et al. [15] employed *node-to-node* penalty-based contact constraints on the cohesive elements, which are applicable only for small sliding displacements. In both the approaches, the contact is enforced through cohesive elements which renders them incapable of handling contact between a cohesive surface and another arbitrarily chosen free surface (see Figure 1b).

The aim of this paper is to present a new framework that couples cohesive zone modeling, representing fracture, and a contact algorithm to handle normal and frictional contact conditions. For this purpose, we employ a *node-to-segment* contact algorithm, with penalty-based constraints. The proposed approach allows for the correct treatment of contact, even for large sliding displacements, thus alleviating the restriction on the cohesive element size: $h < \delta$ is possible without compromising physical parameters. Furthermore, by completely separating the contact treatment from the cohesive elements, the proposed model allows to handle contact between the newly cracked surfaces with any other free surface, such as pre-cracks, external or internal physical boundaries.

This paper starts in Section 2 by describing the methodology employed to couple a *node-to-segment* contact algorithm with cohesive elements. We briefly discuss the *penalty-based* contact formulation employed and describe its use together with the cohesive elements. In Section 3 we validate the proposed model by comparing with results obtained with a Spectral Integral method. We compare the crack kinematics (crack tip position and crack tip velocity) along an interface with and without friction. An excellent match is shown between the results from the proposed numerical model and from the Spectral Integral method. In Section 4 the effect of acknowledging accurately the contact forces during crack propagation is investigated for a non-planar cohesive interface. We

demonstrate that, for such a complex crack path, a small-displacement contact formulation violates the *Karush-Kuhn-Tucker* contact conditions as soon as the cohesive element size becomes comparable to the critical displacement. Finally, in Section 5 we conclude our study by discussing some possible applications of the proposed model, especially in modeling crack propagation along rough surfaces.

All the data and the simulation scripts used in this paper are available on Zenodo [16].

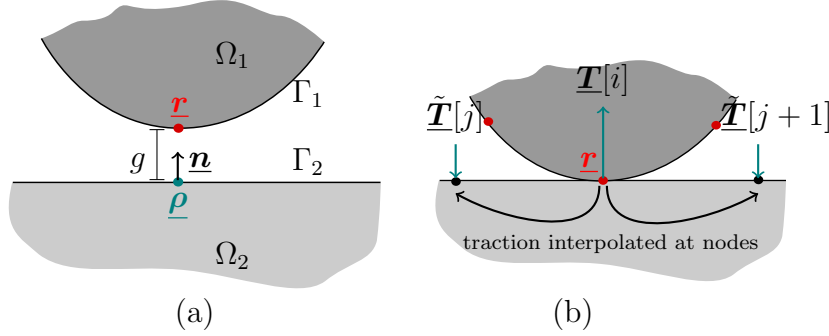## 2. Coupling between cohesive elements and a contact algorithm

Figure 2: (a) A point $\underline{r}$ on a deformable surface Γ_1 is projected onto a surface Γ_2 to compute the gap g. $\underline{\rho}$ is the projection point and $\underline{n}$ is the vector normal to the surface Γ_2 (b) A node from surface Γ_1 in contact with surface Γ_2. The contact traction at the node i is $\underline{T}[i]$ and the interpolated tractions at the nodes of the connected element is $\underline{\tilde{T}}[j]$ and $\underline{\tilde{T}}[j+1]$

Let us consider two deformable bodies Ω_1 and Ω_2 with their boundaries represented as Γ_1 and Γ_2 (see Figure 2a). During the motion of the deformable bodies, portions of Γ_1 and Γ_2 may come into contact. A point $\underline{r}$ on Γ_1 is considered in contact with Γ_2 if the distance to Γ_2, i.e. the gap g, is zero. Once in contact, a point cannot cross the surface Γ_2 and thus, the following constraint is imposed on the surface points of Γ_1,

$$g = (\underline{r} - \underline{\rho}).\underline{n} \geq 0 \tag{5}$$

where $\underline{\rho}$ is the orthogonal projection of $\underline{r}$ onto Γ_2 and $\underline{n}$ is the unit vector normal to the surface, measured at the projection point $\underline{\rho}$ (see Figure 2a). A compressive pressure $N \leq 0$ develops where contact occurs to prevent surface penetration of Γ_1 into the surface Γ_2. Such constraints may be viewed as *Karush-Kuhn-Tucker*(KKT) complementary conditions:

$$g \geq 0, \quad N \leq 0, \quad N \cdot g = 0 \tag{6}$$

When a tangential traction develops along the contacting surface in the presence of friction, the tangential traction $\underline{T}^t$ cannot exceed the critical friction stress according to Coulomb's friction law, which is proportional to the contact pressure N. Assuming a constant friction coefficient μ, the slip motion has to be co-linear to the tangential traction:

$$||\underline{T}^t|| \leq \mu|N| \qquad \text{and} \qquad \underline{v}_\rho = \eta \frac{\underline{T}^t}{||\underline{T}^t||} \tag{7}$$

4

where $\underline{\boldsymbol{v}}_\rho$ is the tangential velocity of the projection point, and where η is the intensity of the slip velocity, which can be viewed as a Lagrange multiplier enforcing the inequality constraint of eq. (7). If a contacting point has a traction $||\underline{\boldsymbol{T}}^t||$ smaller than $\mu|N|$, it sticks to the contacting surface and $\eta = 0$. Otherwise η needs to be determined.

In this work a penalty-based method [17, 18] is employed to regularize the normal and frictional conditions along the contact area. The normal traction N is modified to be a linear function of the gap, and the frictional constraint of eq. (7) classically becomes [19, 20, 21, 22]:

$$\underline{\boldsymbol{T}}^n = \epsilon_n g \underline{\boldsymbol{n}} \qquad \text{and} \qquad \underline{\boldsymbol{v}}_\rho - \eta \frac{\underline{\boldsymbol{T}}^t}{||\underline{\boldsymbol{T}}^t||} = -\frac{1}{\epsilon_t}\frac{d\underline{\boldsymbol{T}}^t}{dt} \tag{8}$$

where the penalty parameters are noted ϵ_n and ϵ_t. For a Finite Element analysis, contact occurs between discretized surfaces and therefore contact can be defined and detected in different ways: *node-to-node*, *node-to-segment* or *segment-to-segment*. In this work, we adopt the *node-to-segment* approach which, as the name suggests, implies that the contact occurs between the nodes of a surface and the segments of another surface. Conventionally, one surface is chosen as the slave surface and the other as the master. A slave node is then matched with an element from the master surface. However, the choice of master and slaves is not unique and may introduce a bias. Furthermore, in a complex crack network with multiple branch sub-cracks and where self-contact could occur, it becomes impossible to identify unambiguously two unconnected surfaces and to distinguish a slave from a master. Therefore, in this work, we define a unique *potential contacting surface* Γ_{det}, containing all the free boundaries. The sets $\mathcal{N}_{det}$ and $\mathcal{E}_{det}$ are the nodes and elements discretizing this surface respectively. Henceforth, contact may occur between the nodes in $\mathcal{N}_{det}$ and the elements in $\mathcal{E}_{det}$. Matching any node with an element is performed by searching for the closest node-segment orthogonal distance:

$$\arg\min_{e\in\mathcal{E}_{det}} \left\{ g = (\underline{\boldsymbol{r}} - \underline{\boldsymbol{\rho}}^e).\underline{\boldsymbol{n}}^e \right\}, \quad \underline{\boldsymbol{r}} \in \mathcal{N}_{det} \tag{9}$$

where $\underline{\boldsymbol{\rho}}^e$ is the orthogonal projection of the node onto element e and $\underline{\boldsymbol{n}}^e$ is the unit vector normal to the element e measured at the projection point $\underline{\boldsymbol{\rho}}^e$. For any node of index i in $\mathcal{N}_{det}$, the discrete traction field $\underline{\boldsymbol{T}}$ can be interpolated onto the nodes of the matching element (see Figure 2b) to provide another measure $\tilde{\underline{\boldsymbol{T}}}$. In order to disambiguate the computation of nodal tractions, the average force between $\underline{\boldsymbol{T}}$ and $\tilde{\underline{\boldsymbol{T}}}$ is assigned to every node in $\mathcal{N}_{det}$. Algorithm 1 summarizes the averaging process employed to compute contact tractions along the nodes of Γ_{det}, which is a classical resolution on contact traction[17].

Thanks to the generality of the contact algorithm described above, it can be applied to the cohesive surfaces created during fracturing. Cohesive elements are inserted during crack growth, and new facets are therefore exposed as free surfaces, as illustrated in Figure 3a. Therefore with each cohesive element i introducing a pair of facets (Γ_i^+, Γ_i^-), the set of potential contacting surface has to be extended:

$$\Gamma_{det} = \bigcup_i \{\Gamma_{det} \cup \Gamma_i^+ \cup \Gamma_i^-\} \tag{10}$$

If all cohesive element facets are candidates to contact pairing, there is nothing preventing to pair a node with the facets immediately connected to this same node (the

---

Algorithm 1 Contact Traction algorithm

    Compute slave traction at node $\underline{\boldsymbol{r}}$

1: **for all** $i \in \mathcal{N}_{det}$ **do** $\triangleright$ Loop over all nodes in Γ_{det}

2:      $e^{\text{closest}}[i] \leftarrow \arg\min\{g = (\underline{\boldsymbol{r}}_i - \underline{\boldsymbol{\rho}}^e).\underline{\boldsymbol{n}}^e\}$ $\triangleright$ Orthogonally closest element to $\underline{\boldsymbol{r}}$

3:      Computes $\underline{\boldsymbol{T}}[i]$ from eq. (8).

    Interpolate traction to the master nodes elements

4: **for all** $i \in \mathcal{N}_{det}$ **do** $\triangleright$ Loop over all nodes in Γ_{det}

5:      **for all** $j \in e^{\text{closest}}[i]$ **do** $\triangleright$ Loop over all the nodes of element e^{closest}

6:          $\underline{\tilde{\boldsymbol{T}}}[j] = \underline{\tilde{\boldsymbol{T}}}[j] - N^j(\underline{\boldsymbol{\rho}}_i)\underline{\boldsymbol{T}}[i]$ $\triangleright$ N^j is the jth shape function

    Average contributions

7: **for all** $i \in \mathcal{N}_{det}$ **do**

8:      $\underline{\boldsymbol{T}}[i] = (\underline{\boldsymbol{T}}[i] + \underline{\tilde{\boldsymbol{T}}}[i])/2$ $\triangleright$ Average traction on i^{th} node

---

orthogonal gap g between a node and an element connected to it is trivially zero). Hence, the elements directly connected to the tested node are simply discarded.

Another misleading situation can arise when a node is closer to a facet element even-though bulk matter is standing between them. This is illustrated in Figure 3b where a node from a cohesive surface Γ_1^+ may be paired with an element from surface Γ_2^-, which belongs to a different crack opening. Again such a facet needs to be discarded from the list of candidates for pairing. By assuming a homogeneous discretization, two cohesive surfaces have to be separated by the characteristic finite element length h_{min}. Therefore, ignoring candidate elements at an orthogonal distance greater than h_{min} will prevent such a wrong node-facet pairing. In Figure 3b are indicated with red crosses the elements that cannot be paired with the node pointed by a red bullet.

A novel modeling aspect is introduced when a cohesive surface enters in contact with another one: the contribution to tractions may come from both the TSL and the contact penalty constraints. Figure 4 illustrates a typical mixed-mode loading of a cohesive surface Γ_{coh} and its facets $\Gamma^{\pm}$. Let us consider two elements e_1, e_2 connected through the cohesive element c_e, which will initiate a crack upon normal loading as shown in Figure 4b. Under tangential loading, the two facets may eventually interpenetrate. When contact constraints are enforced by the TSL, the traction forces issued from the direction of the cohesive spring are unrelated with the actual surface geometries (see Figure 4c). With the proposed algorithm, the element e_1 is projected onto the surface Γ^-, making the contact and the frictional forces consistent with its topology, i.e. the normal (resp. tangential) tractions are normal (resp. tangent) to Γ^-. If the cohesive element is not fully damaged (*i.e* $\delta < \delta_c$), the tractions computed from the TSL are superposed with contact forces, as shown in Figure 4d. In order to clarify the physical origin of this statement, it is important to realize that the cohesion between facets is due to connecting fibers/springs which gradually damage from elongation. The critical elongation δ_c to achieve full rupture is a characteristic of the material, a priori unrelated with the Finite Element mesh: such fibers continue to create an opening resistance until full rupture, and this is to be dissociated from contact forces preventing interpenetration of bulk parts. With the pro-
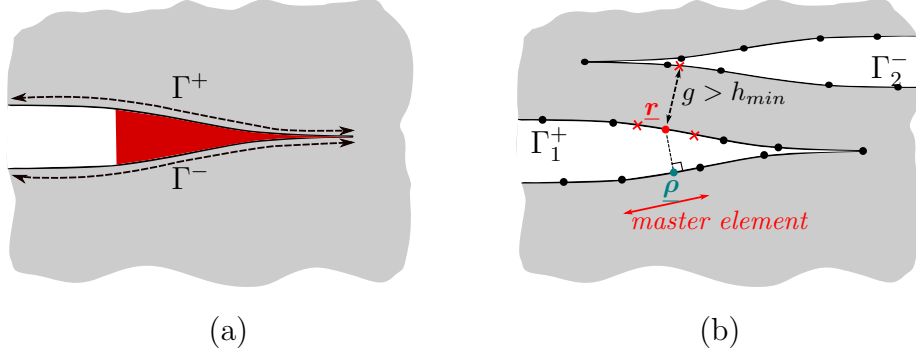
Figure 3: Detection of master element surface when multiple cohesive surfaces exist. Γ_1 and Γ_2 are two cohesive surfaces growing simultaneously which can come in contact with itself. The surface is discretized using finite elements. The slave node $\underline{r}$ is shown in red and the elements connected are discarded as pointed with red crosses. The orthogonal gap between master element and $\underline{r}$ must also be greater than the minimum element size h_{min}. The shown projection ρ is the only one remaining valid.

posed approach, the stresses developing along a crack are not suffering from discretization limitations.

The time evolution in this work will be controlled by a central difference time-integrator[23], which is a modified Newmark-β time integration scheme. At the predictor stage, free surfaces are allowed to interpenetrate, leading to contact penalty forces, while the corrector updates the velocities. The application of such a time integration scheme is known to be unstable[17] when dealing with asymmetric contact constraints. This is a manifest of high frequency oscillations initiating from contacting nodes which will exponentially increase in magnitude. Over the years, various stabilization solutions have been proposed, for instance by introducing local damping [24, 17] or by modifying the velocity/acceleration update of contacting nodes [25, 26]. As the latter solution is applicable only for a *node-to-node* contact algorithm, a kinetic energy damping acting only on the nodes involved by contact constraints is used in the current work. High frequency oscillations can also be created during the dynamic insertion of *extrinsic* cohesive elements (see Appendix A for more details). Again a damping is introduced, for the nodes connected to such newly inserted cohesive elements, in order to reduce the impact of such oscillations.

The above proposed hybrid numerical framework has been implemented with the open-source Finite-Element library Akantu [27]. In the following section, we validate the proposed numerical framework by studying the propagation of a crack along an interface with and without friction.

3. Numerical validation

For the validation of the proposed model, we study the propagation of a crack along a prescribed interface lying within an isotropic elastic body. We consider an infinite elastic space with a finite center-crack of length $2a$ as illustrated in Figure 5a. The system is quasi-statically loaded in mixed-mode: both a compressive loading (along $y-$axis) and a shear loading (along $x-$axis) are applied. The compressive load is firstly increased for a short duration of time before being maintained constant for the rest of the simulation
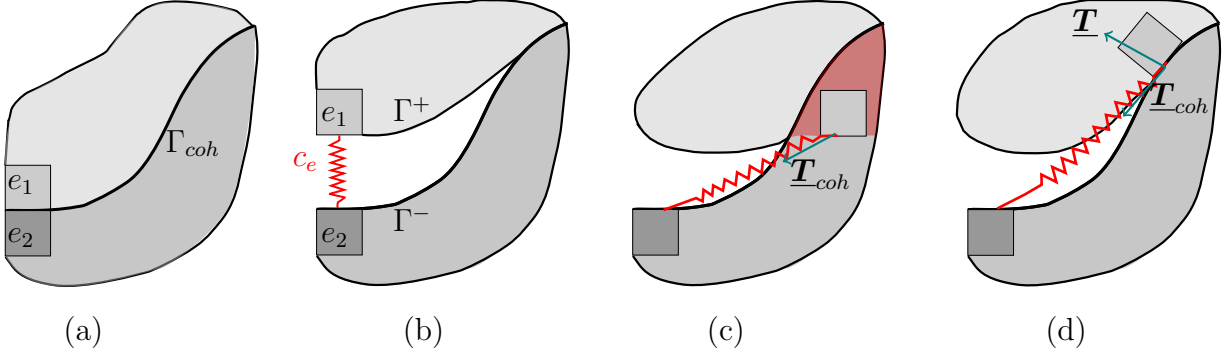
Figure 4: (a) An intact cohesive surface Γ_{coh} (shown in black). The finite elements e_1 and e_2 are joined at the cohesive surface through a cohesive element. (b) The crack opens in mode-I resulting in the formation of two facets Γ^+, Γ^-, connected by the cohesive element c_e represented as a red spring. (c) Upon horizontal displacement the element e_1 crosses Γ^-. Contact constraints are enforced by the cohesive law (d) With large deformation contact forces, provided per the proposed contact algorithm, the element e_1 is projected onto Γ^-. Enforcement of contact and frictional constraints leads to tractions $\underline{T}$ at the facet of the element e_1. As the cohesive element c_e is still active, forces $\underline{T}_{coh}$ also act on the element e_1.

	Isotropic body		Cohesive interface	
Elastic modulus, E	70 MPa	Fracture energy, G_c	20 J/m^2
Poisson's ratio, ν	0.35	Critical strength, σ_c	0.4 MPa
Density, ρ	1230 kg/m^3	Critical opening, δ_c	1×10^{-4} m
Shear wave speed, c_s	145 m/s	β	1
Pressure wave speed, c_d	240 m/s	κ	1

Table 1: Material properties

(see Figure 5a). The shear load also ramps up to a maximum shear stress, chosen to be greater than the critical stress value ($\sigma_{crit} = \sqrt{G_c E / \pi a (1-\nu)}$ [28]) necessary for a crack propagation to initiate under Mode-II loading. The loading ramp applies for a total duration $T = 0.02$ second as shown in Figure 5a. A detailed description and justification for such a ramp function is provided in Appendix B. The material properties of the elastic body and of the cohesive interface are listed in Table 1. The friction acting on the interface is governed by the Coulomb's law with the same static and kinetic coefficients.

3.1. Numerical setup: Finite Element method

This crack configuration is simulated with Finite Element simulations discretizing finite spaces surrounding the crack (see Figure 5). The infinite body is emulated by imposing time-dependent displacements $u_x(t), u_y(t)$ on the boundaries. These are the displacements resulting from a finite crack within an infinite space under mixed Mode-I and Mode-II loadings [29, 28] due to far-field stresses $\sigma_{xy}^\infty(t), \sigma_{yy}^\infty(t)$. For details please refer to Appendix C.

Cohesive elements are dynamically inserted along the crack interface Γ_{coh} during the simulation. A linear TSL describes the crack interface cohesion (see Table 1). For this study, the material parameters G, E, σ_c are chosen such that the fracture process zone
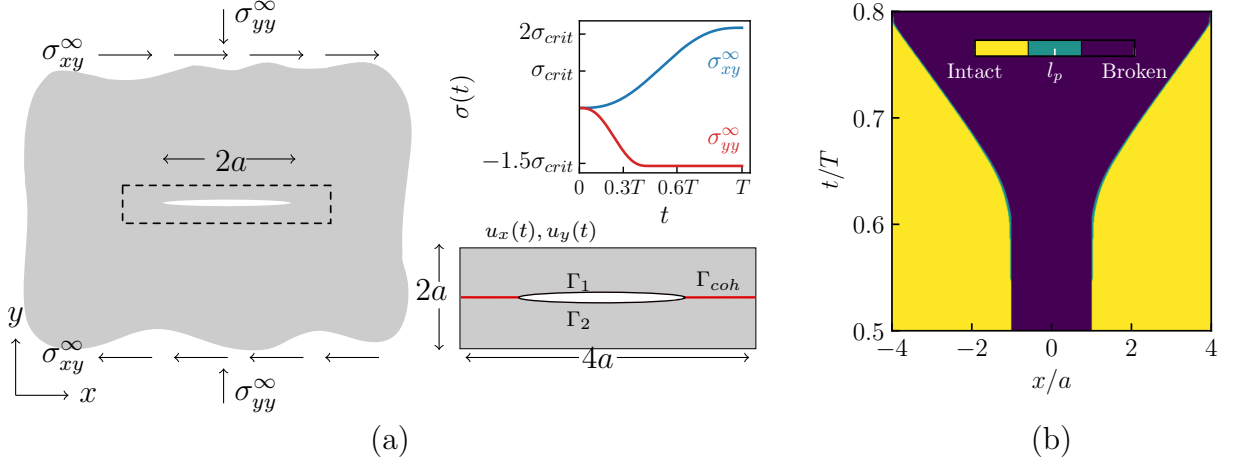
Figure 5: (a) Schematic for an infinite body with a center-crack of length $2a$. The far-field compressive stress σ_{yy}^{∞} and shear stress σ_{xy}^{∞} are quasi-statically applied as shown in the figure. A sub-section of dimension $4a \times 2a$ and crack length $2a$ is considered for Finite Element simulations. The physical boundaries of the center-crack are represented as Γ_1, Γ_2. The cohesive interface where crack will propagate is represented as Γ_{coh}. The Dirichlet boundary conditions are applied along the outer boundary. (b) The space-time representation of the damage is shown for $\mu = 0.3$ and $\epsilon_n = \epsilon_t = 300E$. The blue region represents the broken part, the green region represents the *fracture process zone* and the yellow part represents the unbroken region.

$l_p = EG_c/\sigma_c^2 = 100\delta_c = 4a/50$ [30] which satisfies $\delta_c < l_p < 4a$. The lower limit $\delta_c < l_p$ ensures that an appreciable cohesive zone develops ahead of the crack while the upper limit $l_p < 4a$ ensures that the cohesive zone remains small if compared to the domain dimensions. Thus the displacement field applied on the boundary is expected to remain a valid approximation. The *fracture process zone* must contain enough finite elements (at-least around four [31]) to correctly capture the non-linear stresses nearby the crack tip. To this end, a structured mesh consisting of bi-linear elements of uniform size ($h = l_p/10$) is employed.

In the problem described above, the potential contacting surfaces are Γ_1, Γ_2 and the upper and the lower facets ($\Gamma_{coh}^+, \Gamma_{coh}^-$) to be created during the crack propagation. Thus it allows to define:

$$\Gamma_{det} = \Gamma_1 \cup \Gamma_2 \cup \Gamma_{coh}^+ \cup \Gamma_{coh}^- \qquad (11)$$

To enforce contact constraints along the potential contacting surface, various values of the penalty parameter ϵ_n are considered while the frictional penalty ϵ_t is chosen equal to ϵ_n. The system is solved using the explicit damping scheme presented in last section. In principle the critical time step Δt_{crit} is chosen based on the Courant-Freidrichs-Lewy condition: $\Delta t_{\text{crit}} = \alpha h_{\min}\sqrt{\rho(1-\nu^2)/E}$, where α is a security factor, $h_{\min}$ is the minimum element size, E is the *Young's modulus* of the material and ν is its Poisson's ratio [32]. However, Δt_{crit} also depends on the choice of the penalty parameter ϵ_n: enforcing contact constraints through penalty-based methods decreases the stable time step [33, 34]. In this

work, it is chosen according to [33]:

$$\Delta t = h_{\min}\sqrt{\frac{\rho(1-\nu^2)}{E}}\sqrt{\frac{2}{1+\beta+\sqrt{1+\beta^2}}}, \quad \beta = \frac{\epsilon_n h_{\min}}{EA} \tag{12}$$

where A is the area associated with surface nodes. The nodes in contact or belonging to a cohesive element are damped by velocity scaling to stabilize the simulation (1% of velocity amplitude every time step).

Finite Element predictions of the proposed model will be compared with the ones obtained with a Spectral Integral method [9, 10] available as an open-source software [35]. In the following section, we briefly describe the Spectral Integral method and the numerical setup employed.

3.2. Numerical setup : Spectral Integral method

The Spectral Integral approach discretizes only tractions and displacements along the interface between two semi-infinite continua, for which the elasto-dynamics are treated implicitly. For a 2D isotropic solid, the tractions at the interface are governed by:

$$\boldsymbol{T}^{\pm}(x,t) = \boldsymbol{T}^{\infty\pm}(t) - \frac{E}{2(1+\nu)c_s}\frac{\partial \underline{\boldsymbol{u}}^{\pm}}{\partial t}(x,t) + \underline{\boldsymbol{f}}^{\pm}(x,t) \tag{13}$$

where $\boldsymbol{T}^{\infty\pm}(t)$ corresponds to the far-field loading $[\sigma_{xy}^{\infty}(t)\ \sigma_{yy}^{\infty}(t)]^T$, $\underline{\boldsymbol{u}}^{\pm}$ corresponds to the displacements of the upper(+) and the lower facets(−) of an interface and $\underline{\boldsymbol{f}}^{\pm}$ represents history-dependent tractions. For a detailed description of the method, the readers should refer to [9, 35]. Tractions and displacements are solved in a hybrid Fourier-Laplace space (spatial-time) and therefore periodicity conditions apply on the spatial domain. The infinite body problem described in Section 3 is emulated by considering a center-crack of length $2a$ within a periodic domain of length $30a$. Such a large domain ensures that the periodicity does not spuriously affect the crack initiation and propagation. The interface is discretized with regular element of size approximately equal to $l_p/10$. An explicit time stepping scheme is employed with a time step Δt_{crit} equal to the one used for the Finite Element simulations.

Similarly to the previously described Finite Element approach, the interface strength is described by a linear TSL which couples normal and shear decohesion. After the failure, the interpenetration between the facets of the interface is handled by matching the normal displacements along the upper and the lower faces: this effectively sets the gap as $g = 0$. Along the interface, a Coulomb friction law is employed with a simplified Prakash regularization [36, 37]:

$$\frac{d\tilde{\sigma}_{yy}}{dt} = \frac{1}{t^{\star}}(\tilde{\sigma}_{yy} - \sigma_{yy}) \tag{14}$$

where $\tilde{\sigma}_{yy}$ is the regularized compressive stress while σ_{yy} is the instantaneous compressive stress at the interface and $t^{\star}$ is the regularization characteristic time. The justification of this regularization can be found in the experimental work of [36] where it is shown that frictional stresses cannot change instantaneously in reaction to sudden jumps in the compressive stresses. The time $t^{\star}$ quantifies the delay reaction of the frictional stress

response ($\mu|\tilde{\sigma}_{yy}|$), which should eventually correspond to the Coulomb strength [38]. Thus, the tangential traction along the interface is limited by the frictional stress given as:

$$||\underline{\boldsymbol{T}}^t|| \leq \mu|\tilde{\sigma}_{yy}| \tag{15}$$

In the next section, we compare results for the crack propagation as predicted by the FE approach and the Spectral approach. However, there are few conceptual differences between the two approaches that must be taken into consideration. The TSL employed in Spectral method, although similar to FE approach, does not acknowledges the irreversible damage during unloading and therefore, requires the applied loading to be monotonically increasing. Also, the response of frictional stress in the Spectral approach is non-instantaneous to any change in compressive stress and therefore, the compressive stress must not change drastically during the crack propagation. Still, the characteristic time $t^\star$ was chosen much lower than the loading ramp rate, so that it is not expected to impact the measured results or the comparison with Finite Elements by any means. As it will be seen, it stabilizes the progression of the crack, making Finite Element result slightly more noisy. Taking these two things in considerations, we simulated the propagation of crack under mixed-mode loading and the results are presented and compared in the next section.

3.3. Validation results

The simulations are run for two different friction coefficients: $\mu \in [0, 0.3]$. Normal and frictional contact constraints are tested with penalty parameters $\epsilon_n = \epsilon_t = 300E$ which prooved to be sufficient to reach a convergence with respect to normal and tangential tractions at the contacting interface. More results for $\epsilon_n = \epsilon_t \in [100E, 200E]$ can be found in Appendix D. Figure 5b shows a space-time diagram of the damage as predicted by the finite element method (for $\mu = 0.3$). The crack propagation initiates at $t/T \approx 0.6$ and accelerates before reaching a steady-state velocity.

Foremost, we show the interpenetration that remains between the contacting surface after the enforcement of constraints (for $\mu = 0.3$). Figure 6a shows the space-time representation of the interpenetration gap (g), which is evaluated from the upper crack face ($\Gamma_1 \cup \Gamma_{coh}^+$). Before the start of the crack propagation ($t/T < 0.6$), contact occurs only along Γ_1. Later as the crack propagates, the contact occurs across both Γ_1 and Γ_{coh}^+. During the entire simulation, the maximum interpenetration value is quite small, below 0.004% of the crack size and therefore can be considered as an acceptable error in KKT conditions.

In the presence of friction, tangential tractions develop along the contacting surface which govern the relative motion of the contacting surfaces. Figure 6c shows the average normal and tangential tractions ($\bar{T}^n$ and $\bar{T}^t$) developed along the surface for $\mu = 0.3$ and $\epsilon_t = 300E$. $\bar{T}^n$ is expected to saturate to the applied normal stress σ_{yy}^∞ while $\bar{T}^t$ should saturate to the corresponding frictional stress $\mu\sigma_{yy}^\infty$. It can be seen that both the normal tangential tractions converge to the expected values (indicated by horizontal dashed lines in Figure 6c). Figure 6b shows the space-time representation of the ratio $||\underline{\boldsymbol{T}}^t||/||\underline{\boldsymbol{T}}^n||$ along the contacting surface. At the beginning, the contacting surface sticks $i.e$ the ratio between the tangential traction and the normal traction is less than the friction coefficient μ. As the load increases, the traction ratio increases and leads to a transition from sticking to slipping when $t/T \sim 0.3$ (shown as a white line in Figure 6b and as a vertical dashed
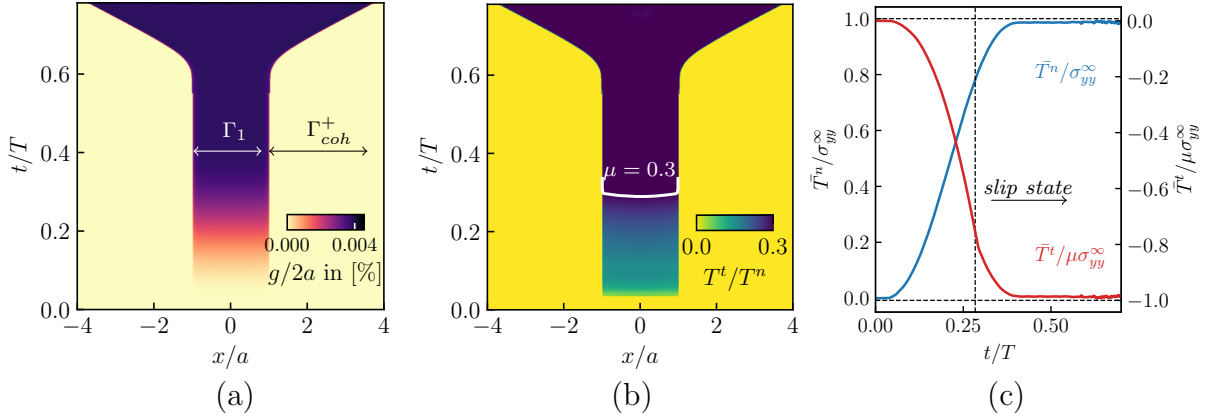
Figure 6: (a) Space-time diagram for the interpenetration value g for the case: $\mu = 0.3$ and $\epsilon_n = \epsilon_t = 300E$. The interpenetration value is below 0.004% of the crack length at any time. The crack position is normalized by half of the crack length and the time is normalized by the total time (b) Space-time diagram for the ratio between $||\underline{\boldsymbol{T}}^t||$ and $||\underline{\boldsymbol{T}}^n||$ for the case: $\mu = 0.3$ and $\epsilon_n = \epsilon_t = 300E$. The white line represents the moment when ratio is equal to the friction coefficient $\mu = 0.3$. The contact surfaces are in slip state above the white line. (c) Evolution of the average normal traction and the average tangential traction along the contacting surface. The dashed horizontal lines represents the expected values of the normal traction and the tangential traction at the interface.

line in Figure 6c). Thus, at the time of initiation the two surfaces are slipping and continue slipping while the crack propagates.

Next, we compare the crack propagation obtained with Finite Elements to the Spectral Integral method. Figure 7a shows the crack tip position as a function of time for two different values of μ. For $\mu = 0$, the crack propagation as predicted by the Spectral method starts earlier than with Finite Elements. The delay in the initiation is believed to be linked to the necessary time for stress waves to travel through the Finite Element body. Indeed, for the Spectral Integral method the applied far-field stress is instantaneously impacting the interface whereas for Finite element simulations some time is required for the applied stress to redistribute in the body and reach the interface. The delay between the two initiation events is $\Delta t/T = 0.017$ which is close to the traveling time of a stress wave from the top boundary to the crack tip ($a/c_d T = 0.021$, where a is one-half of the height of the domain and c_d is the speed of the dilatation wave).

In the presence of friction, the residual tractions act in the direction opposite to the shearing direction which reduces the Mode II stress concentration at the crack-tip. In order to initiate the propagation, the net stress must be higher than the critical stress (σ_{crit}), therefore appearing as a delay in the crack propagation. In Figure 7a, such an effect of μ onto the crack propagation is demonstrated. As expected both FEM and Spectral approaches predict a delay of the crack propagation onset if compared to friction-less cases. Dynamical effects again lead to an observable delay between FE and Spectral predictions which is equal to the minimum time required for stress waves to traverse the half the bulk domain. The slight differences between analytic and predicted delays ($0.017T$ and $0.024T$) is believed to result from high frequency oscillations present in the cohesive zone which cause small fluctuations of the critical stresses close to the crack tip (more details
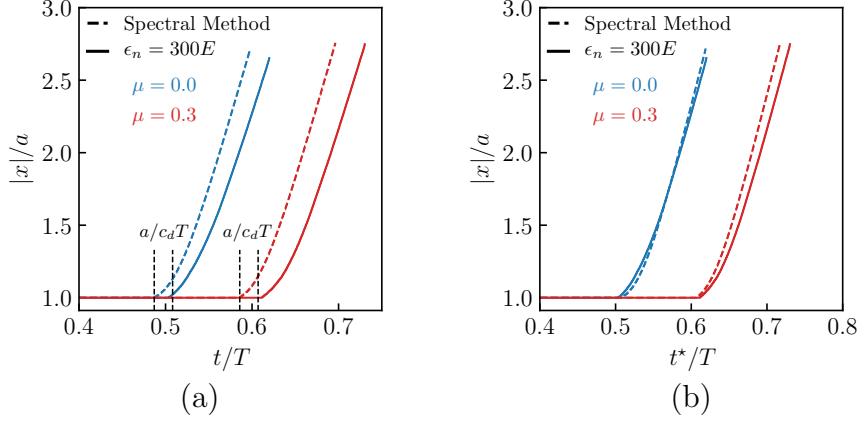
12

Figure 7: (a) Crack tip positions as a function of time for various values of friction coefficient. The dotted lines (blue, red) show the predictions of the Spectral Integral method. The vertical dashed lines show the minimum time required for the stress waves to reach crack tip from the top boundary. (b) Crack tip positions after shifting the Spectral Integral results from Figure 7a by $a/c_d T$.

in Appendix A). For a better comparison, the crack tip positions predicted from Spectral Integral are shifted by the analytical delay $a/c_d T = 0.021T$ in Figure 7b: the predictions from both methods are matching well except for some details in the propagation front velocity.
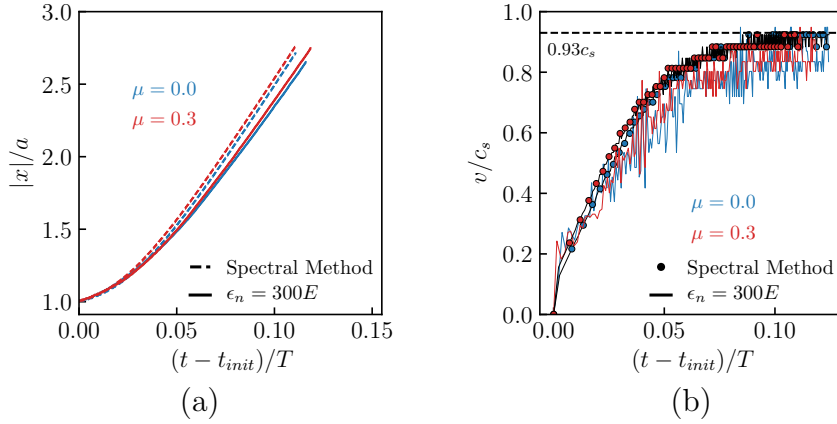

Figure 8: (a) Crack tip positions after setting to a common origin. The dotted lines show the predictions of the Spectral Integral method. (b) Crack tip velocities as a function of time for different friction coefficients.

Shifting the crack positions to a common origin allows to compare the respective crack tip velocities in Figure 8a and Figure 8b. The cracks predicted with FE are slower than their Spectral Integral counter-part as visible in both Figure 8a and Figure 8b. This must be due to the slight damping employed to stabilize the explicit time integration scheme. Nevertheless, setting aside the delay observed in the crack propagation and the slightly lower velocity, the FE predictions match particularly well the expected evolution, with first a strong acceleration before reaching a saturation to the steady-state *Rayleigh* wave speed, which is the thermo-dynamically admissible limit for Mode II cracks (with

Isotropic body		Weak Interface		Strong Interface	
Elastic modulus, E	7 MPa	Fracture energy, G_c^w	20 J/m^2	G_c^s	200 J/m^2
Poisson's ratio, ν	0.35	Critical strength, σ_c^w	0.04 MPa	σ_c^s	0.4 MPa
Density, ρ	1230 kg/m^3	Critical opening, δ_c^w	1×10^{-3} m	δ_c^s	1×10^{-3} m
		β^w	1	β^s	1
		κ^w	1	κ^s	1

Table 2: Material properties

$c_r \approx 0.93 c_s$ for the considered material properties). The crack tip velocities predicted from our approach show fluctuations (see Figure 8b) believed to be caused by slight interpenetration remaining between surfaces (see Figure 6a) which is further aggravated by the oscillations from dynamic insertion of cohesive elements. The issue of interpenetration between surfaces can be addressed by means of the augmented Lagrangian method [21]. It would require several iterations within each time-step to enforce constraints perfectly and thus would become computationally costly especially in a multiple-cracks setting. Because the presented results are mainly satisfactory, it was decided not to *augment* the contact resolution.

Notwithstanding the slight interpenetration of the surfaces, the results from our hybrid approach show an excellent match with Spectral Integral results. The capability of the hybrid approach to enforce contact between cohesive surfaces as well as pre-existing surfaces is very well demonstrated in the above section. However, as mentioned earlier, the potential of this work is when large relative displacement may occur. While a Spectral Integral approach can produce accurate results in this case, it requires a flat interface by construction. Next section will put our method to the test with a cracking interface following a sinusoidal curve, and with large relative displacement of crack lips.

4. Influence of contact enforcement methods on crack propagation

This section scrutinizes the influence that the contact algorithms have on the crack propagation. The hybrid cohesive-contact numerical model is compared with the more common approach where cohesive elements also resolve for contact penalty. The aim is to demonstrate that the presented hybrid approach can palliate numerical issues appearing when the critical displacement is larger than the characteristic mesh size, i.e. $h \leq \delta_c$. Similarly to the previous section, we consider an infinite isotropic elastic body with a finite size center-crack of length $2a$. The crack propagation is limited along a cohesive interface Γ_{coh} which now follows a sinusoidal path as shown in Figure 9a. The material properties of the elastic body are given in Table 2, and the cohesive properties are chosen such that the sinusoidal interface is weaker than the planar interface ($G_c^s = 10 G_c^w$, $\sigma_c^s = 10 \sigma_c^w$) so as to initiate crack propagation along the sinusoidal interface first. Again the system is quasi-statically loaded: tensile loading (along y−axis) and shear loading (along x−axis). The tensile load $\sigma_{yy}^\infty(t)$ is applied for a short duration and is then maintained throughout the simulation. The shear load $\sigma_{xy}^\infty(t)$ is increased throughout the simulation (see Figure 9a). The maximum shear load is chosen to be greater than the critical strength of the strong interface, in order for the crack to reach and start propagating within the strong interface. The loads are applied for a total duration $T = 0.06$ second as shown in the Figure 9a.
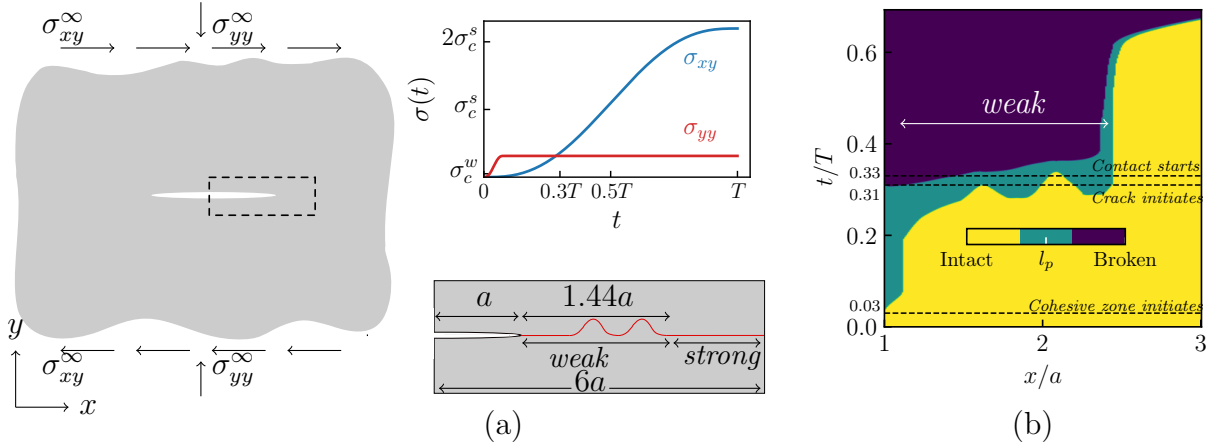
14

Figure 9: (a) Schematic of a infinite body with a center-crack of length $2a$. The body is loaded quasi-statically under far-field tensile stress σ_{yy}^∞ and shear stress σ_{xy}^∞ as shown in the figure. A sub-section of finite dimensions $6a \times 2a$ is considered with a crack length of a and a sinusoidal path for crack propagation. The cohesive interface Γ_{coh} is made up of a weak interface (sinusoidal profile) and a strong interface (planar profile). The sinusoidal profile follows $y = \lambda/2 \sin(\pi x/\lambda)$ with a wavelength $\lambda = a/2$. (b) Space-time representation of crack propagation. The blue region represents the broken part, the green region represents the *fracture process zone* and the yellow part represents the unbroken region

4.1. Numerical setup

Similar to Section 3.1, a finite size sub-section from an infinite body is considered (see Figure 9a) and the displacements, corresponding to the far-field tensile and shear loads, are applied along the boundary.

A linear TSL is employed to describe the cohesive behavior between the two interfaces. The cohesive properties are chosen such that the critical displacement is the same for the entire cohesive interfaces and satisfies $\delta_c^w = \delta_c^s = l_p^s/10$. The fracture process zone sizes for the strong and weak interfaces are $l_p^s = 6a/75$ and $l_p^w = 10 l_p^s$ respectively. A structured mesh consisting of bi-linear elements of uniform size $h = \delta_c^s$ is used for both cases. In the above problem, the *potential contacting surface* is emerging after opening of the weak cohesive interface and therefore, is defined as:

$$\Gamma_{det} = \Gamma_{weak}^+ \cup \Gamma_{weak}^- \tag{16}$$

The contact penalty ϵ_n is chosen identical for the standard and hybrid cohesive methods. An explicit Newmark-β time integration scheme is again employed, with the critical time step Δt_{crit} and the damping force chosen as in previous section.

4.2. Comparison results

Figure 9b shows the space-time representation of the crack propagation for the standard contact formulation. As expected the weak interface starts damaging first (at $t/T = 0.03$ the initiation of cohesive zone in the weak interface) when Mode-I loading is dominant (see loading curve Figure 9a). The crack propagation starts much later at $t/T \sim 0.31$ and continues along the weak interface before arresting when reaching
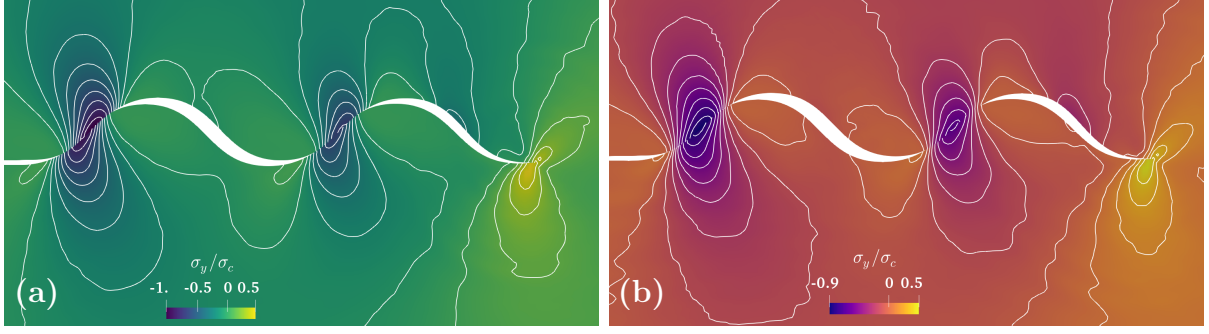
Figure 10: Snapshots of stress σ_y and stress contours around the crack interface for (a) Default contact formulation for cohesive elements. (b) Proposed contact formulation for cohesive elements. The snapshots are at time $t/T \sim 0.5$. The stresses are normalized by the critical strength of the strong interface.

the strong interface ($x/a = 2.44$). The facets of the weak cohesive surface become in contact at $t/T \sim 0.33$, leading to the development of residual stresses behind the crack tip. Figure 10 shows the snapshots of the stress field σ_y at $t/T \sim 0.5$ as predicted by the standard cohesive-element model and the hybrid cohesive-contact model. As mentioned earlier, when contact tractions are handled with the TSL, the contact detection is fundamentally facet-to-facet. The interpenetration is therefore checked between pairs of facets, which are associated during the setup of the simulation. A sliding over a distance larger than h across a non-planar topology may lead to faulty situations where the two facets are physically distant from each other, but would still be accounted as in contact by computing a negative opening δ_n. Figure 11c and Figure 11d illustrate this issue, by highlighting elements connected to $\Gamma^{\pm}$ which were initially facing each other and therefore forming a contact pair. After a substantial sliding they wrongly interact with each other through the cohesive TSL by computing a negative δ_n, and leading to the development of spurious tangential forces. Therefore it becomes possible that contact tractions do not coincide with the contact areas, which violates the *Kuhn-Tucker* complementary conditions. This appears as a spurious shift in the stress field, visible in Figure 10a, whereas the accurate treatment of contact made with the hybrid approach is consistent as presented in Figure 10b. This is also illustrated in Figure 11a and Figure 11b where the stress σ_y is plotted along one of the contacting areas. The shaded zone indicates where cohesive facets are in contact, which again reveals that positive tractions are computed in non-contacting regions with the standard formulation. Conversely, stresses and the contact zone do coincide when employing our hybrid approach.

The improper treatment of contact affects the residual stresses developed behind the crack tip. Figure 12 shows the average residual stress $\bar{\sigma}$ developed along the shear direction, which was integrated over the length of the weak interface:

$$\bar{\sigma} = \frac{\int_{\Gamma_{coh}^+} \underline{\underline{\sigma}}(x,y).\underline{n}(x,y).\underline{e}_x dA}{1.44a}, \ a \leq x \leq 2.44a \tag{17}$$

where $\underline{\underline{\sigma}}$ is the stress tensor field, and $\underline{n}$ is the vector normal to Γ_{coh}^+. The cohesive-contact numerical model predicts a larger residual stress if compared with the hybrid approach. This difference in residual stresses will aggravate for rougher cohesive-contact surfaces, as it is the case for fractured concrete [39]. Furthermore, the lower residual stress predicted
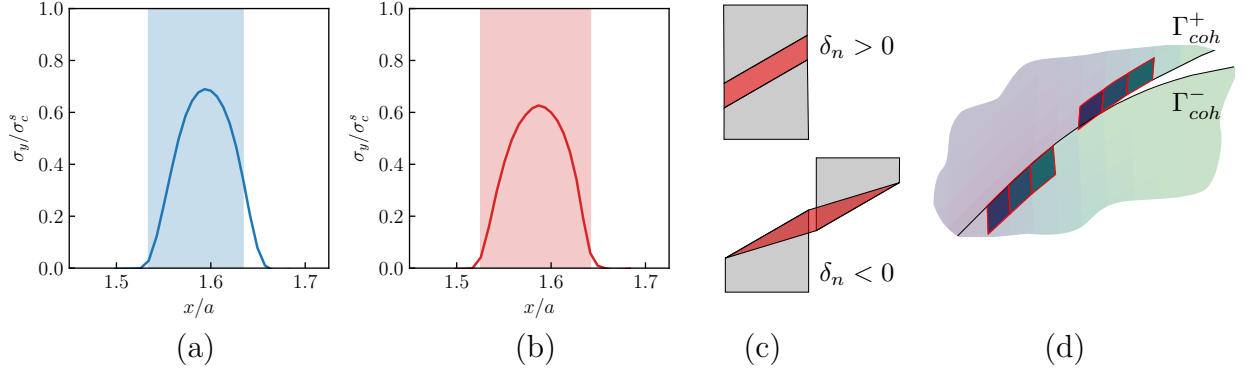
Figure 11: Stresses along the contacting region are shown for (a) Default contact formulation (b) Proposed contact formulation. The shaded region in both the figures represent the contacting region. (c) A schematic showing the condition where the two facets of a cohesive element are not in contact but $\delta_n < 0$. (d) A zoomed view around the contacting region shows the finite elements violating the Kuhn-Tucker condition. The highlighted elements connected to $\Gamma_{coh}^{\pm}$ were initially facing each other at the onset of the simulation.
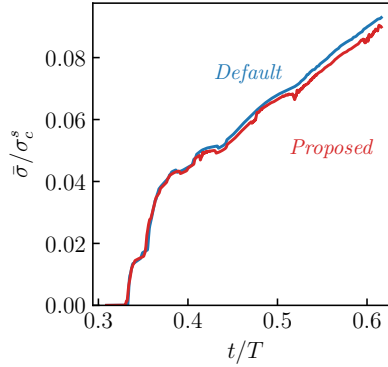

Figure 12: Residual stresses developed due to the contact between the facets of the weak cohesive interface.

with the hybrid model leads to a lesser shear resistance, leading in turn to the earlier propagation of the crack tip as seen in Appendix E. The above comparison highlights the importance of KKT conditions on the crack propagation. Unlike the contact enforcement with the cohesive law, the KKT conditions are always satisfied for our hybrid approach and thus ensures a more accurate prediction of the crack behavior.

5. Conclusion

In this work, we presented a hybrid cohesive-contact approach to study the simultaneous process of fracture and of contact between fracturing surfaces. An *extrinsic* cohesive element strategy is employed to model the fracture and a *penalty-based* method is used to enforce contact and frictional constraints. This was motivated by the necessity to describe fracture for sliding displacements greater than the characteristic mesh length. We validated the proposed model by comparing with the Spectral Integral method, which is known to deliver accurate results for a planar interface[35]. The crack kinematics (tip

17

position and velocity) predicted with the two methods match quite well for surfaces with friction and without friction, which validated our approach in the case of a flat crack path.

Then it was shown that the traditional approach of enforcing contact constraints through cohesive elements suffers from several limitations: the facet-to-facet strategy, with contacting facets being paired during simulation setup, is independent of any relative displacement. In the case where free surfaces are non-planar and/or when the sliding displacement is larger than the characteristic element size, it leads to inaccurate contact areas and contact tractions. The proposed hybrid-cohesive-contact method adopts a *node-to-segment* contact detection which allows a correct enforcement of contact constraints even at large sliding displacements and does not restrict the size of the elements, since contact pairs are regularly updated. This allows for an arbitrary refinement, e.g. with cohesive elements becoming smaller than the critical displacement. Separating the contact resolution from the calculation of cohesive forces allows to study complex crack networks, self-interacting by interlocking and friction mechanisms.

This study confirms that a correct resolution of contact constraints is crucial to achieve an accurate modeling of fracture mechanisms. It is believed that the proposed model will open the path to a more reliable and physically-based study of crack path roughness, where fine elements are required to model small scale topological features. Rough surfaces issued from fractures possess height variations which can be at the μ-scale, e.g. for PMMA [40], concrete [39] and many other materials [41]. Furthermore, materials such as concrete or PMMA have critical displacements in the order $\sim$ 10-100 μm [42, 43, 35]. This would require the cohesive elements to be smaller than the characteristic length and would justify an usage of our hybrid approach. The presented method would also allow to study the propagation of cracks along surfaces with interlocking protuberances such as aggregates and re-bars in concrete [44, 45, 46] or for bio-inspired sutures [47, 48]. These are forming an active field of research, since interlocking mechanisms introduce a resistance to crack propagation which can increase the effective material strength.

6. Acknowledgment

Appendix A. High frequency oscillations in extrinsic cohesive elements

In *extrinsic* approach, the stresses from the adjoining elements are interpolated onto the quadrature points of facets and if the stress at any one of the quadrature points exceeds the critical stress, a cohesive element is suddenly inserted. The initial opening δ at each quadrature point is computed from the quadrature point stresses:

$$\delta_q = \frac{\sigma_c}{\sigma_q}\delta_c, \quad \text{where } \sigma_q = \text{ stress at quadrature point } q \tag{A.1}$$

In the case where there is a stress variation along the cohesive interface, the cohesive element will have varying openings and tractions.

These opening oscilations characteristic of extrinsic cohesive elements are shown after the sudden insertion due to a homogeneous tensile load. The displacements are slowly imposed along the upper and the lower boundaries of the body as shown in Figure A.13a, and the cohesive elements are inserted dynamically along Γ_{coh} when the critical stress is reached. Figure A.13b and Figure A.13c shows a snapshot after the cohesive insertion of the variation in damage and normal opening along Γ_{coh}. The 2% variation proves the presence of oscillations along the cohesive surface, which also alters the interface tractions (see Figure A.13d). Furthermore, the oscillations in coheisve opening and thus in coheisve tractions results in variation in the stress fields (around 2%) along the surface (see Figure A.13e).
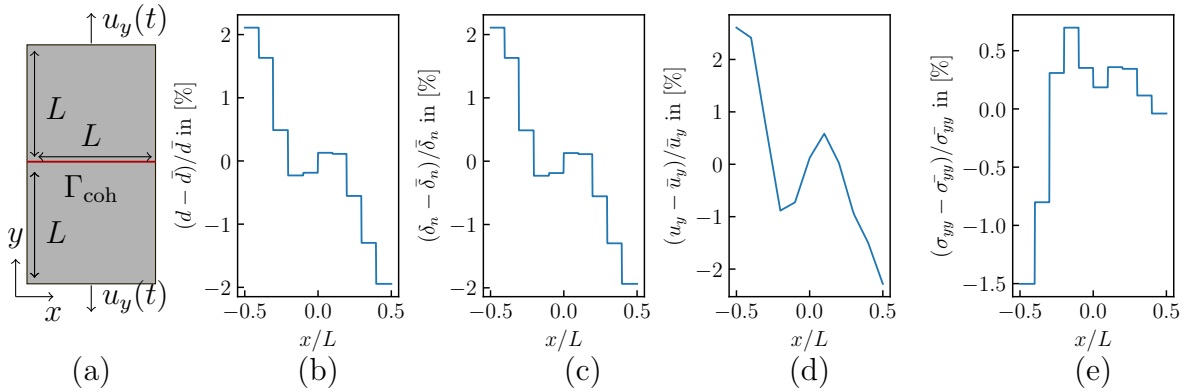

Figure A.13: (a) An elastic body loaded quasi-statically in Mode-I under plain strain conditions. The material parameters are : E, ρ and $\nu = 0$. The boundaries of the body are constrained along $x-$ axis. Various quantities computed along the cohesive interface (b) Variation in damage along the cohesive surface (c) Variation in normal opening (d) Variation in displacements along $y-$axis of the nodes at Γ_{coh} (e) Variation in stresses σ_{yy} along the cohesive surface

Appendix B. Quasi-static loading

In this study, since the quasi-static behavior is simulated by employing an explicit time-integration scheme therefore the inertial effects needs to be minimized. This is achieved by maintaining the ratio of kinetic energy to internal energy below 5% during the simulation. As the dominant response of a quasi-static analysis is the first fundamental

mode, therefore the loads are applied for a total duration $2T$ where T is the time period for the first natural frequency of the model and 2 is the security factor. Furthermore, the loads are increased as smoothly as possible to avoid any sudden propagation of stress wave due to instantaneous loading. To achieve this, the total loading $\sigma(T)$ is divided into n time steps $(n = T/\Delta t_{crit})$ and load at i^{th} time step is given by the polynomial function:

$$\sigma(t_i) = \sigma(0) + (\sigma(T) - \sigma(0))t_i^3(10 - 15t_i + 6t_i^2), \quad t_i = i\Delta t_{crit} \tag{B.1}$$

As the Finite Element simulations are displacement controlled, therefore displacements corresponding to $\sigma(t_i)$ are applied at time step t_i along the boundaries. Figure B.14 shows the internal and the kinetic energies computed for the problems described in Section 3 and Section 4. As can be observed the simulations can be considered as quasi-static as the kinetic energies are very small compared to the internal energies.
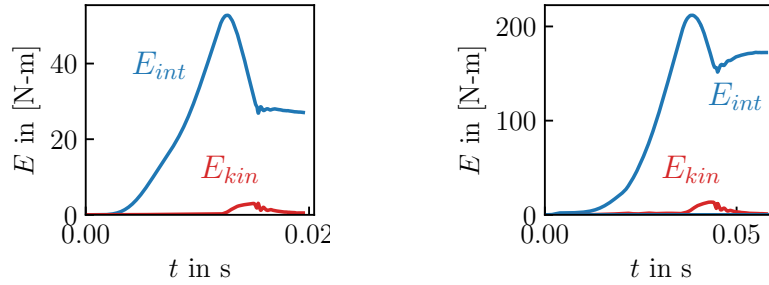

Figure B.14: (a) Internal energy E_{int} and Kinetic energy E_{kin} for problem described in Section 3. The energies shown are predicted with Finite Element simulations for $\mu = 0.3$ and $\epsilon_n = 300E$. (b) Internal energy E_{int} and Kinetic energy E_{kin} shown for problem described in Section 4.

Appendix C. Mixed Mode : Full displacement field

Using principle of superposition, the stress field for mixed-mode loading can be computed as [29, 28, 49]:

$$\sigma_{xx} = \underbrace{\text{Re}\phi' - y\text{Im}\phi''}_{\text{Mode-I}} + \underbrace{2\text{Re}\psi' - y\text{Im}\psi''}_{\text{Mode-II}} \tag{C.1}$$

$$\sigma_{yy} = \underbrace{\text{Re}\phi' + y\text{Im}\phi'' + \sigma_{yy}^{\infty}}_{\text{Mode-I}} + \underbrace{-y\text{Im}\psi''}_{\text{Mode-II}} \tag{C.2}$$

$$\sigma_{xy} = \underbrace{-y\text{Re}\phi''}_{\text{Mode-I}} + \underbrace{-\text{Im}\psi' - y\text{Re}\psi'' + \sigma_{xy}^{\infty}}_{\text{Mode-II}} \tag{C.3}$$

where

$$\phi' = \frac{\sigma_{yy}^{\infty}z}{\sqrt{z^2 - a^2}} - \sigma_{yy}^{\infty}, \quad \psi' = -i\frac{\sigma_{xy}^{\infty}z}{\sqrt{z^2 - a^2}} + i\sigma_{xy}^{\infty} \tag{C.4}$$

$$\phi'' = (\frac{1}{\sqrt{z^2 - a^2}} - \frac{z^2}{\sqrt{z^2 - a^2}})\sigma_{yy}^{\infty}, \quad \psi'' = -(\frac{1}{\sqrt{z^2 - a^2}} - \frac{z^2}{\sqrt{z^2 - a^2}})\sigma_{xy}^{\infty}i \tag{C.5}$$

20

Thus, the displacement fields at point $(z = x + iy)$ computed from the superposed stress state for a plain strain condition can be expressed as [29, 28]:

$$2\mu u_x = \underbrace{(1 - 2\nu)\text{Re}\phi - y\text{Im}\phi^{'}}_{\text{Mode-I}} + \underbrace{2(1 - \nu)\text{Re}\psi - y\text{Im}\psi^{'} + 2y\sigma_{xy}^{\infty}}_{\text{Mode-II}} \tag{C.6}$$

$$2\mu u_y = \underbrace{2(1 - \nu)\text{Im}\phi - y\text{Re}\phi^{'} + (1 - \nu)y\sigma_{yy}^{\infty}}_{\text{Mode-I}} + \underbrace{(1 - 2\nu)\text{Im}\psi - y\text{Re}\psi^{'}}_{\text{Mode-II}} \tag{C.7}$$

The above displacement fields are adjusted to generate interfacial stresses similar to the Spectral integral method. By the construction of Spectral Integral method, under mixed-mode loading the compressive stress along the interface are always constant and equal to the applied compressive stress σ_{yy}^{∞} (remains unaffected by the shear loading) and the shear stress along the interface are representative of pure Mode-II loading. Thus, the new displacements field applied along the boundaries are given as:

$$2\mu u_x = 2(1 - \nu)\text{Re}\psi - y\text{Im}\psi^{'} + 2y\sigma_{xy}^{\infty} \tag{C.8}$$

$$2\mu u_y = (1 - \nu)y\sigma_{yy}^{\infty} \tag{C.9}$$

Appendix D. Effect of penalty parameter

The problem in Section 3 is tested with different values of penalty parameters: $\epsilon_n = \epsilon_t = 100E, 200E, 300E$. Here we present the effect of penalty parameter on the interpenetration value, the average normal traction and the average tangential traction. Figure D.15 shows the effect of penalty parameter on the interpenetration value along the contacting surface at $t/T = 0.6$. With no contact tractions, $i.e.$ $\epsilon_n = 0$, the interpenetration can reach a high 0.08% of the crack size. As ϵ_n is increased, the interpenetration reduces drastically ($< 0.02\%$) and reaching as low as 0.004% of the crack size for $\epsilon_n = 200E$ and $\epsilon_n = 300E$. As mentioned earlier, the interpenetration value will tend to 0 as $\epsilon_n \rightarrow \infty$. Therefore, a convergence in interpenetration gap is hardly expected. However, as $g \rightarrow 0$, the normal traction must tends towards the applied normal stress. Figure D.15c and Figure D.15d shows the convergence for the normal and the tangential traction for the problem in Section 3. For $\epsilon_n = \epsilon_t = 300E$, the normal and the tangential traction are converged to the expected values.

Appendix E. Effect of residual stresses on crack propagation

Improper treatment of contact also affects the crack propagation. Here we demonstrate the crack propagation for the problem described in Section 4. Figure E.16 shows the position of crack and cohesive zone tips for the cohesive-contact numerical model and the hybrid cohesive-contact model presented in this paper. The tip positions are shown only for the strong interface (for $x/a \geq 2.44$).
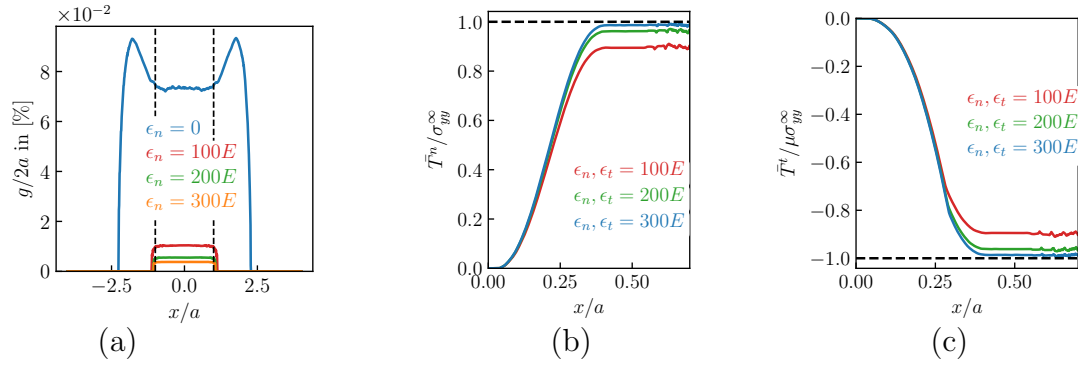
Figure D.15: (a) Effect of penalty parameter on the interpenetration value across the contacting surface for the problem discussed in Section 3. (b) Average normal traction computed along the contacting surface for different values of penalty parameter (c) Average tangential traction computed along the contacting surface for different values of penalty parameter
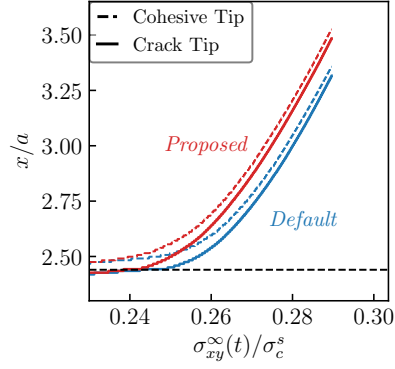

Figure E.16: The evolution of the crack tip and the cohesive tip as function of far-field shear stress σ_{xy}. The strong interface starts at $x/a = 2.44$ shown by the dotted black line.

References

[1] A. A. Griffiths, VI. The phenomena of rupture and flow in solids, Philos. Trans. R. Soc. London. 221 (582-593) (1921) 163–198, The Royal Society London, 1921. `doi:10.1098/rsta.1921.0006`.

[2] G. I. Barenblatt, The Mathematical Theory of Equilibrium Cracks in Brittle Fracture, Adv. Appl. Mech. 7 (C) (1962) 55–129, Elsevier, 1962. `doi:10.1016/S0065-2156(08)70121-2`.

[3] T. Camacho, M. Ortiz, Computational modelling of impact damage in brittle materials, Int. J. Solids Struct. 33 (2) (1996) 2899–2938, 1996. `doi:10.1016/0020-7683(95)00255-3`.

[4] M. Ortiz, A. Pandolfi, Finite-deformation irreversible cohesive elements for three-dimensional crack-propagation analysis, Int. J. Numer. Methods Eng. 44 (9) (1999) 1267–1282, 1999. `doi:10.1002/(SICI)1097-0207(19990330)44:9<1267::AID-NME486>3.0.CO;2-7`.

[5] L. Snozzi, J.-F. Molinari, A cohesive element model for mixed mode loading with frictional contact capability, Int. J. Numer. Methods Eng. 93 (5) (2013) 510–526, John Wiley & Sons, Ltd, 2013. `doi:10.1002/nme.4398`.

[6] R. De Borst, Numerical aspects of cohesive-zone models, Eng. Fract. Mech. (70) (2003) 1743–1757, 2003. `doi:10.1016/S0013-7944(03)00122-X`.

[7] M. Vocialta, N. Richart, J.-F. F. Molinari, 3D dynamic fragmentation with parallel dynamic insertion of cohesive elements, Int. J. Numer. Methods Eng. 109 (12) (2017) 1655–1678, John Wiley & Sons, Ltd, 2017. `doi:10.1002/nme.5339`.

[8] C. V. Verhoosel, R. De Borst, A phase-field model for cohesive fracture, Int. J. Numer. Methods Eng. 00 (2010) 1–20, 2010. `doi:10.1002/nme`.

[9] M. S. Breitenfeld, P. H. Geubelle, Numerical analysis of dynamic debonding under 2D in-plane and 3D loading, Int. J. Fract. 93 (1-4) (1998) 13–38, 1998. `doi:10.1023/a:1007535703095`.

[10] P. H. Geubelle, D. V. Kubair, Intersonic crack propagation in homogeneous media under shear-dominated loading: Numerical analysis, J. Mech. Phys. Solids 49 (3) (2001) 571–587, Pergamon, 2001. `doi:10.1016/S0022-5096(00)00041-7`.

[11] X. P. Xu, A. Needleman, Numerical simulations of fast crack growth in brittle solids, J. Mech. Phys. Solids 42 (9) (1994) 1397–1434, Pergamon, 1994. `doi:10.1016/0022-5096(94)90003-5`.

[12] O. Ylmaz, J. F. Molinari, A mesoscale fracture model for concrete, Cem. Concr. Res. 97 (2017) 84–94, Elsevier Ltd, 2017. `doi:10.1016/j.cemconres.2017.03.014`.

[13] D. S. Kammer, V. A. Yastrebov, G. Anciaux, J. F. Molinari, Journal of the Mechanics and Physics of Solids The existence of a critical length scale in regularised friction, J. Mech. Phys. Solids 63 (2014) 40–50, Elsevier, 2014. `doi:10.1016/j.jmps.2013.10.007`.

[14] F. Cirak, M. West, Decomposition contact response (DCR) for explicit finite element dynamics, Int. J. Numer. METHODS Eng. Int. J. Numer. Meth. Engng 64 (2005) 1078–1110, 2005. `doi:10.1002/nme.1400`.

[15] S. Zhang, S. Mohadeseh, T. Mousavi, N. Richart, J.-F. Molinari, K. Beyer, Micromechanical finite element modeling of diagonal compression test for historical stone masonry structure, Int. J. Solids Struct. 112 (2017) 122–132, 2017. `doi:10.1016/j.ijsolstr.2017.02.014`.

[16] M. Pundir, Supplementary data to 'Coupling between cohesive element method and Node-to-segment contact algorithm : Implementation and application'2020. `doi:10.5281/zenodo.4293497`.

[17] T. A. Laursen, Computational contact and impact mechanics : fundamentals of modeling interfacial phenomena in nonlinear finite element analysis, Springer, Berlin, 2002.

[18] V. Yastrebov, Computational contact mechanics : geometry , detection and numerical techniques École doctorale n O 432 : Sciences des Métiers de l ' Ingénieur THÈSE l ' École nationale supérieure des mi2012.

[19] A. Konyukhov, K. Schweizerhof, Contact formulation via a velocity description allowing efficiency improvements in frictionless contact analysis, Comput. Mech. 33 (3) (2004) 165–173, 2004. `doi:10.1007/s00466-003-0515-3`.

[20] A. Konyukhov, K. Schweizerhof, Covariant description for frictional contact problems (2005) 190–2132005. `doi:10.1007/s00466-004-0616-7`.

[21] J. C. Simo, T. A. Laursen, An augmented lagrangian treatment of contact problems involving friction, Comput. Struct. 42 (1) (1992) 97–116, 1992. `doi:10.1016/0045-7949(92)90540-G`.

[22] N. Kikuchi, J. T. Oden, Contact Problems in Elasticity: A Study of Variational Inequalities and Finite Element Methods, pp. 1–17. `doi:10.1137/1.9781611970845.ch1`.

[23] T. Belytschko, The Finite Element Method: Linear Static and Dynamic Finite Element Analysis: Thomas J. R. Hughes, Comput. Civ. Infrastruct. Eng. 4 (3) (1989) 245–246, 1989. `doi:10.1111/j.1467-8667.1989.tb00025.x`.

[24] K. Schweizerhof, Efficiency Refinements of Contact Strategies and Algorithms in Explicit Finite Element Programming (April 1992), 2018.

[25] R. L. Taylor, P. Papadopoulos, On a finite element method for dynamic contact/impact problems, Int. J. Numer. Methods Eng. 36 (12) (1993) 2123–2140, 1993. `doi:10.1002/nme.1620361211`.

[26] T. J. Hughes, R. L. Taylor, J. L. Sackman, A. Curnier, W. Kanoknukulchai, A finite element method for a class of contact-impact problems, Comput. Methods Appl. Mech. Eng. 8 (3) (1976) 249–276, 1976. `doi:10.1016/0045-7825(76)90018-9`.

[27] N. Richart, J.-F. Molinari, Implementation of a parallel finite-element library: Test case on a non-local continuum damage model.

[28] T. L. Anderson, Fracture Mechanics : Fundamentals and Applications, Vol. 88, Taylor & Francis Group, 1996.

[29] H. Westergaard, Bearing Pressures and Cracks (1939).

[30] A. Hillerborg, M. Modéer, P. E. Petersson, Analysis of crack formation and crack growth in concrete by means of fracture mechanics and finite elements, Cem. Concr. Res. 6 (6) (1976) 773–781, 1976. `doi:10.1016/0008-8846(76)90007-7`.

[31] L. Snozzi, A. Caballero, J. F. Molinari, Cement and Concrete Research In fl uence of the meso-structure in dynamic fracture simulation of concrete under tensile loading, Cem. Concr. Res. 41 (11) (2011) 1130–1142, Elsevier Ltd, 2011. `doi:10.1016/j.cemconres.2011.06.016`.

[32] K. Friedrichs, On the Partial Difference Equations (March) (1967) 215–234, 1967.

[33] T. Belytschko, M. O. Neal, Contact-impact by the pinball algorithm with penalty and Lagrangian methods, Int. J. Numer. Methods Eng. 31 (3) (1991) 547–572, 1991. `doi:https://doi.org/10.1002/nme.1620310309`.

[34] P. Wriggers, Computational contact mechanics, second ed., Springer, 2006. `doi:10.1007/978-3-540-32609-0`.

[35] F. Barras, When dynamic cracks meet disorder: A journey along the fracture process zone 8956 (2018) 191, 2018.

[36] V. Prakash, Frictional Response of Sliding Interfaces Subjected to Time Varying Normal Pressures 1 (January), 1998.

[37] A. M. Rubin, J.-P. Ampuero, Aftershock asymmetry on a bimaterial interface 112 (May) (2007) 1–23, 2007. `doi:10.1029/2006JB004337`.

[38] A. Cochard, J. R. Rice, Fault rupture between dissimilar materials : Ill-posedness , regularization , and slip-pulse response 105, 2000.

[39] M. Pundir, G. Anciaux, Numerical generation and contact analysis of rough surfaces in concrete, hal-025734812020.

[40] S. Vernède, L. Ponson, J.-p. Bouchaud, Turbulent Fracture Surfaces : A Footprint of Damage Percolation ? 215501 (May) (2015) 1–5, 2015. `doi:10.1103/PhysRevLett.114.215501`.

[41] B. N. J. Persson, O. Albohr, U. Tartaglino, A. I. Volokitin, E. Tosatti, On the nature of surface roughness with application to contact mechanics, sealing, rubber friction and adhesion., J. Phys. Condens. Matter 17 (1) (2005) R1–R62, 2005. `doi:10.1088/0953-8984/17/1/R01`.

[42] P. Ba, H. M. Asce, Q. Yu, Size-Effect Testing of Cohesive Fracture Parameters and Nonuniqueness of Work-of-Fracture Method 137 (1983) (2011) 580–588, 2011. `doi: 10.1061/(ASCE)EM.1943-7889.0000254`.

[43] I. Carol, C. M. Lã, Micromechanical analysis of quasi-brittle materials using fracture-based interface elements 215 (2001) 193–215, 2001. `doi:10.1002/nme.277`.

[44] M. Tirassa, M. Fernández Ruiz, A. Muttoni, Influence of cracking and rough surface properties on the transfer of forces in cracked concrete, Eng. Struct. 225 (February) (2020) 111138, Elsevier, 2020. `doi:10.1016/j.engstruct.2020.111138`.

[45] M. Pundir, M. Tirassa, M. Fernández, A. Muttoni, G. Anciaux, Review of fundamental assumptions of the Two-Phase model for aggregate interlocking in cracked concrete using numerical methods and experimental evidence Tensile reinforcement, Cem. Concr. Res. 125 (August) (2019) 105855, Elsevier, 2019. `doi:10.1016/j. cemconres.2019.105855`.

[46] M. Tirassa, An interlocking approach for the rebar-to-concrete contact in bond, Mag. Concr. Res.2020. `doi:10.1680/jmacr.20.00209`.

[47] M. Mirkhalaf, A. K. Dastjerdi, F. Barthelat, Overcoming the brittleness of glass through bio-inspiration and micro-architecture, Nat. Commun. 5 (2014) 1–9, Nature Publishing Group, 2014. `doi:10.1038/ncomms4166`.

[48] P. D. Zavattieri, L. G. Hector, A. F. Bower, Cohesive zone simulations of crack growth along a rough interface between two elastic plastic solids 75 (2008) 4309–4332, 2008. `doi:10.1016/j.engfracmech.2007.11.007`.

[49] L. I. Sedov, A course in continuum mechanics, Vol. 4, Groningen, Wolters-Noordhoff., 1972.